IV. Results and Discussion

A. Data Acquisition

Data acquisition and analysis are preformed on Digital VaxStation 4000s, with dedicated Motorola MVME single-card computer front ends attached to CAMAC electronics. The XSYS data acquisition system is used to record the position of each ion that hits the PSD on an event-by-event basis. One-dimensional gates are set on the PSD x-projection spectra, to keep the primary ions, single electron-capture ions, and double electron-capture ions counted separately as a function of the ramp voltage.

The ramp voltage, that governs the ultimate energy of the ions at the time of incidence with the target atoms, is also recorded with the position information for each event. The ramp voltage for a particular event is converted to a collision voltage, and is used to determine the ion energy at the time of the collision.

Typical spectra as they are displayed during a run are shown in **Figure 4.1**, and **Figure 4.2**. In **Figure 4.1**, windows labeled 20, 21, and 22 plot the events for the x, y, and r channels of the PSD, and window 23 is the sum of the x, y and r channels. The window labeled 25 is the two-dimensional position spectra, and window 26 is the x-projection of the two-dimensional position. Before data acquisition, one dimensional gates are set on the x-projection spectra, to bin and separate counts from the primary beam from those of single capture and from double capture. The focusing of the ion beam spots changes very little as the voltage on the **OPIG** is ramped, so the gates only need to be set once per run. The ramp voltage data is sent to the ADC.

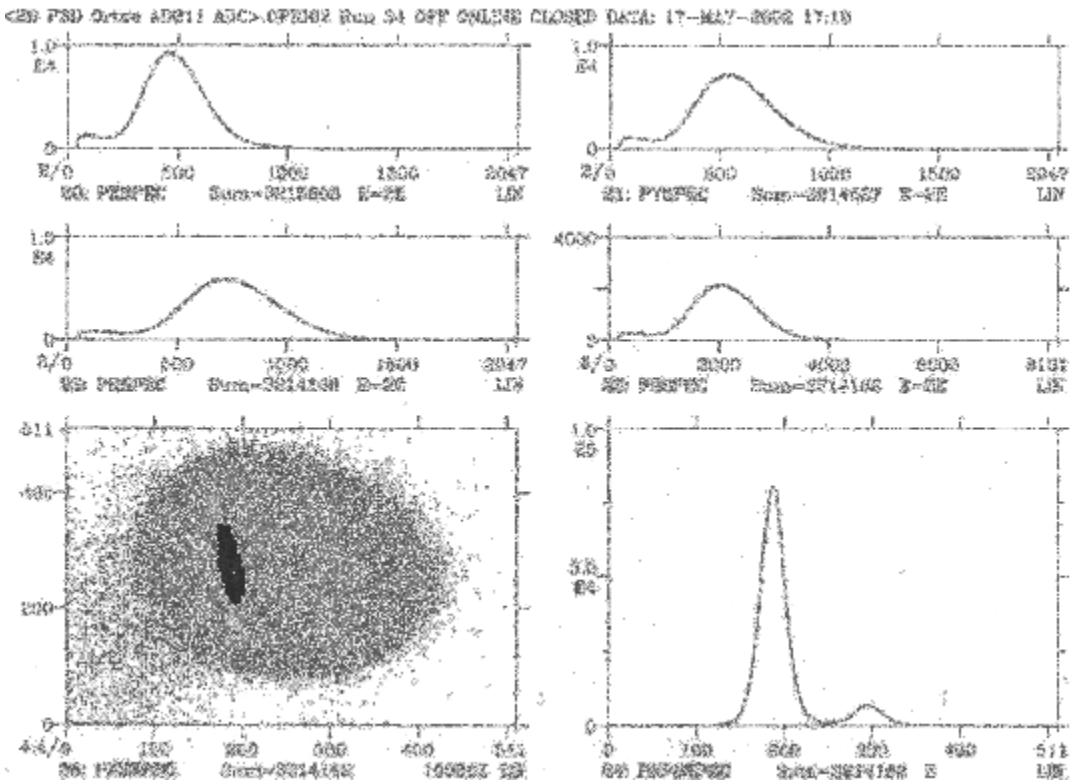

Figure 4.1 Windows showing the x, y, r, sum, 2-dimensional position spectra, and the x projection of the 2-dimensional position spectra on the VAX station with data from a typical measurement displayed.

Spectra for the gated signals that separately count the primary ions, single electron-capture ions, and double electron-capture ions, as well as the sum of the gated signals for the primary ion beam, single capture, and double capture, and one spectrum that is the sum of all counts on the PSD, are all displayed as a function of the ramp voltage on the XSYS screen, and are shown in windows 26-30 respectively, in **Figure 4.2**. The XSYS data analysis code for this procedure is given in **Appendix 2**.

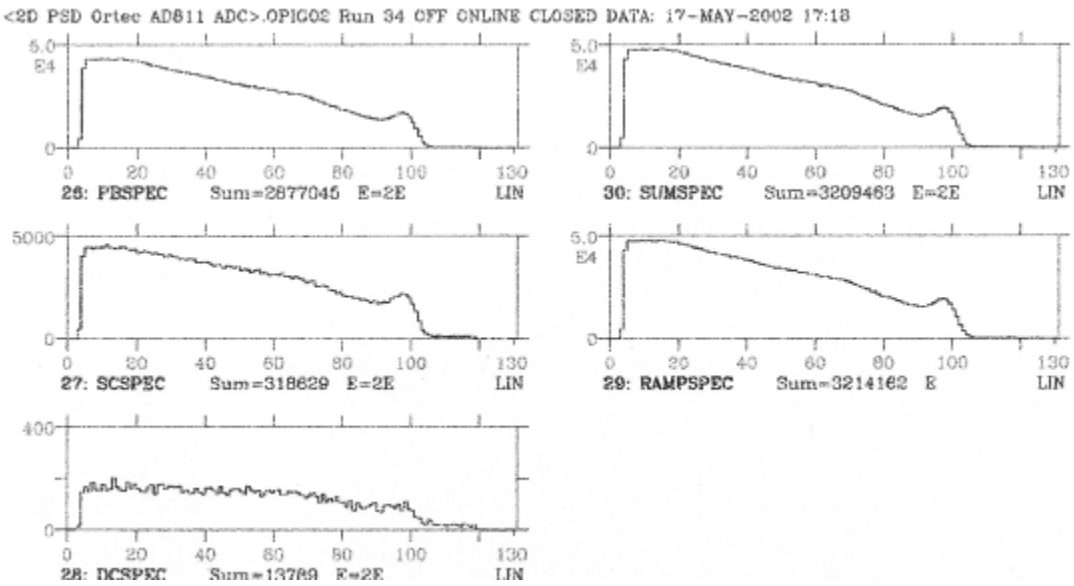

Figure 4.2 Windows showing the gated primary, single capture, double capture, sum, and total counts as a function of ramp voltage, with data from a typical measurement displayed.

The data for the primary ions, single electron-capture ions, and double electron-capture ions as a function of the ramp voltage are saved as .evl files, which can then be FTPed to networked PCs, and saved as ASCII files. The ASCII files are imported into Origin 6.1, where computations are done to obtain single and double electron capture cross sections.

B. Cross Section Determination

The cross sections for electron capture can be obtained from the data using a fairly simple expression. Consider a cylindrical volume element V, with an area A, and length L, with a target gas in this volume. The effective area for electron capture from one atom is a. Also, assuming that there is a uniform flux of ions passing through the

area A, the total number of ions n_{ion}, passing through A, can be related to the number of ions that capture an electron n_{cap}, by

$$\frac{n_{ion}}{A} = \frac{n_{cap}}{Na}, \qquad \textbf{(Eq. 4.1)}$$

where N is the number of target atoms. If we consider the total number of ions passing through the volume V, then **Equation 4.1** can be written as

$$\frac{n_{ion}}{AL} = \frac{n_{cap}}{NaL} \qquad \textbf{(Eq. 4.2)}$$

The effective capture area for a target atom is the capture cross section, s ($a = s$). Solving for the capture cross section gives,

$$s = \frac{n_{cap}AL}{n_{ion}NL} = \frac{n_{cap}V}{n_{ion}NL}. \qquad \textbf{(Eq. 4.3)}$$

Now, using the ideal gas law,

$$\frac{V}{N} = \frac{kT}{P}, \qquad \textbf{(Eq. 4.4)}$$

where P is the pressure, k is Boltzmann's constant (1.38×10^{-23} J/K), and T is the temperature in Kelvin (when calculating cross sections, the temperature, T, was taken as 300 Kelvin, which is roughly room temperature), the cross section can be expressed as

$$s = \frac{n_{cap}kT}{n_{ion}PL}. \qquad \textbf{(Eq. 4.5)}$$

Equation 4.5 is used to calculate the electron capture cross sections, using quantities that are measured in the experiment.

The method used to calculate cross sections, using the data that are imported to Origin 6.1 will now be discussed. From the first run (the primary and single capture beams recorded), the data from spectrum 26, the gated primary beam vs. ramp voltage,

and the data from spectrum 27, the gated single-capture beam vs. ramp voltage are converted to an ASCII file, and exported to Origin. From the second run (single capture and double capture recorded), the gated single-capture beam vs. ramp voltage, and the data from spectrum 28, the gated double-capture beam vs. ramp voltage are also converted to an ASCII file, and exported to Origin.

In Origin, the primary beam vs. ramp voltage spectrum is examined, and the exact ramp voltage which corresponds to a collision energy of zero is determined. The primary beam vs. ramp voltage has a slowly decreasing count rate as the ramp voltage is increased. The ramp voltage that corresponds to half the counts of the maximum of the peak of the cut-off is defined as the ramp voltage that corresponds to a collision energy of 0 eV. Fitting a Gaussian to the derivative of the cut-off curve, and obtaining a "full width at half max." from this fit gives a good estimate of the energy spread of the ion beam as extracted from the **CRYEBIS**.

The amplitude of the peak-to-peak ramp voltage is 150 volts, and there are 128 channels that are used for binning the ramp voltage. The conversion to collision voltage is as follows,

$$V_{Coll} = \text{-ramp-}CH_0 \times 1.1719, \qquad \textbf{(Eq. 4.6)}$$

where each binned channel of the ramp voltage is converted to a collision voltages. In **Equation 4.6**, CH_0 is the channel that is equal to the zero collision voltage, 'ramp' is the binned data from XSYS, and V_{Coll} corresponds to the actual collision voltages.

The next step involves normalizing the double-capture data from the second data (where the single and double-capture beam counts are acquired) to the first data set (where the primary and single-capture beam counts are acquired). The double-capture to

single-capture ratio is obtained for all measured collision voltages by dividing the double-capture from the single-capture from the second data set. The product of this ratio and the single capture count rate from the first run, gives a normalized value for what the double capture would have been the first run (as if it had been measured directly). Essentially, a column for double capture counts is created for the first run.

The counts of the primary, and single-capture from the first run, and the generated double capture counts are added for each channel to obtain a number of total counts as a function of collision energy. Next, the fractions for single-capture to total counts, double-capture to total counts are calculated for each channel. Using these fractions, pressure, and cell length, **Equation 4.5** can be used to calculate the cross section for each corresponding collision voltage.

C. Error Analysis

The total error in the cross sections can be reasonably obtained, by considering the various sources of error, and making the appropriate calculations or estimations for each type of error involved. Some of the sources of error which effect the value of the cross sections are statistical errors, pressure variations and calibration of the pressure meter, as well as differences in the pressure from where the pressure is recorded and the actual pressure inside the gas cell, errors introduced in determining the 'effective' length of the gas cell, improper positioning of the gates which are used to separate the primary beam from the single capture, and double capture beams. Errors in determination of the energy of the collision are inherent in the method that is used to define the collision energy.

Statistical uncertainties for the values of $n_{capture}$ and n_{ion} from **Equation 4.5**, need to be considered when calculating the total capture cross sections. The statistical uncertainties for $n_{capture}$ and n_{ion} are calculated by adding the errors in quadruture. The individual uncertainties for $n_{capture}$ and n_{ion} are

$$\Delta n_{capture} = \sqrt{n_{capture}} \Big/ n_{capture}, \text{ and } \Delta n_{ion} = \sqrt{n_{ion}} \Big/ n_{ion}, \qquad \textbf{(Eq. 4.7)}$$

respectively, and the statistical error in the capture cross section, $_{stat}$, is

$$s_{SCstat} = s_{Capture}\sqrt{(\Delta n_{capture})^2 + (\Delta n_{ion})^2} \qquad \textbf{(Eq. 4.8)}$$

where $\sigma_{Capture}$ is the cross section for electron capture. For most systems measured, the statistical error was quite small, and can be roughly estimated by looking at the fluctuation of the data points. In most cases, the statistical error bars were much smaller than the data points. (The graph showing the plotted single and double electron capture cross sections in **Figure 4.3** has statistical error bars included for the KSU data).

The difference between the actual gas cell length and the "effective" cell length is a combination of two factors. The actual length that the ions traverse from the entrance to exit of the gas cell is slightly longer than the length of the gas cell due to the motion induced in the ions from the *r-f* field on the **OPIG**. The difference in cross section due to this effect was estimated using the same Microsoft Excel spreadsheet that was used to generate the plot shown in **Figure 3.5**. For Ar^{+8} with an axial velocity, $V_z = 6.9 \times 10^5$ cm/sec, and with all other initial conditions identical to the conditions used to generate **Figure 3.5**, the total distance that the ion travels in the gas cell was approximated by adding the distance between the sets of x, y, and z data points for the 15 cm of the **OPIG**, using Pythagorean's theorem. The total distance traveled by an ion, for this simulation

was approximately 15.1 cm, which is less than a 1% difference from the gas cell length. This is a nearly negligible path length increase, and does not significantly change the calculated cross sections from the data taken in this study. The second contribution to error in the effective length of the gas cell is determined by how high the pressure is outside of the gas cell region. Since the gas cell is differentially pumped, and the pressure is much lower (being in the low 10^{-7} Torr pressure range, while the pressure inside the gas cell is of the order of 10^{-5} Torr) outside the gas cell, gas will flow out of the gas cell at the apertures on each end of the cell. The apertures on the entrance and exit ends of the **OPIG** are 1 mm in diameter. The effective gas cell length is taken as 10.5 cm when performing cross section calculations. The estimated absolute error in the target length is ± 2 cm, or roughly 16%.

The pressure in the gas cell was monitored during the course of taking data. The pressure meter was found to display a reading that was higher than the actual pressure (having an offset of about 2.25×10^{-5} mb), which could be easily corrected when calculating cross sections by subtracting off the offset from the displayed reading. The pressure was quite stable, and fluctuated by no more than $\pm 0.1 \times 10^{-5}$ mb, giving an error of approximately ± 5%. Adding all the sources of error in the pressure and target cell length, give approximately 20-25 % absolute error in the value of the cross sections.

All of the errors discussed thus far relate to the error in the value of the cross sections (the y-axis). Another source of error that needs to be considered is the error in the collision energy (or x-axis). Error can be introduced when determining which ramp voltage corresponds to a collision energy of zero eV. A method has been used to determine the zero-collision energy ramp voltage (as discussed in chapter 3). The

greatest limitation in accurately determining the collision energy, is the energy spread of the projectile ions. The energy spread of the projectile ions from the **CRYEBIS** is approximately 4-5 qV/amu. Although the cross sections are plotted at energies down to 0 eV/amu, the collision energy is less clearly defined at energies below this 4-5 qV/amu. To determine the absolute error in the collision energy, we may include an additional ±1 qV/amu, allowing for the possibility of a poor fit, in determining the "center of the cut-off curve" (which will be explained more at the end of the chapter). The total error in the collision energy is approximately 5-6 qV/amu.

D. Experimental Cross-Section Measurements

In general, the total single electron capture cross sections, for basically every measured system (there are a few exceptions), change very little as a function of energy for the range of energies examined. While there has been reason to speculate that the cross section behavior will change for very low collision energies (i.e., strongly polarized targets influencing the projectile trajectory), the results of the present study imply that the dominant capture process is nearly velocity independent. Several decades ago, it was found that the behavior of electron capture cross sections tended to be nearly velocity independent at collision energies ranging from a few hundred to a few thousand eV **[4.1, 4.2, 4.3, 4.4, 4.5]**. The body of data collected in this study suggests that this behavior of the electron capture cross sections can be extended to include collision energies between a few eV to a few hundred eV, and are in relatively good agreement with the extended version of the classical over the barrier model of Neihaus [**4.6**].

Several different ion-atom and ion-molecule systems were measured in this work. There were different reasons that each particular system was chosen for study. Generally, for one ion species, a range of charge states was systematically measured, for a particular target. Some of the systems measured were chosen because other groups had previously measured the same systems, and their results could be used for comparison with the cross sections obtained in this work. In some cases, the systems chosen were simply picked as a representative survey, to demonstrate general cross section trends for different types of collision parameters.

The general trends that have been observed in the cross sections measured in this work, and how they compare with those measured by Okuno et. al. **[4.7]**, as well as the

absorbing sphere model, the scaling law of Müller and Salzborn, and the Langevin model are illustrated in **Figure 4.3**. The three theoretical models shown are only calculated for single electron capture.

The measured total double electron capture cross sections are more difficult to compare with theory because it is complicated to incorporate the Auger electron emission process into a double capture model. Any double capture followed by electron emission is measured as a single capture event for this experiment, and reduces the number of double capture events that are measured. For this reason, the double capture cross sections from this work have only been compared with the double capture cross sections from Okuno et. al. . **[4.7]**.

In general, the single capture cross sections measured for this work were consistent with the scaling law of Müller and Salzborn and the classical over barrier model. (The classical over-barrier model is not shown in the **Figure 4.3** to avoid crowding the figure). Okuno's cross sections tended to agree better with the absorbing sphere model, and Müller and Salzborn's model on the higher energy side, and the Langevin model on the lower energy side of the energy range studied. The single capture cross sections from both Okuno's measurements and this study were greater than the double capture cross sections by about an order of magnitude. Okuno's double capture cross sections also increased with decreasing collision energy, while our double capture cross sections were more flat. For some situations, the single and/or double electron capture cross sections of this study did change slightly with energy, but did not change nearly as much as those measured by Okuno.

While it's difficult to explain the differences between Okuno's cross section measurements from the cross sections measured in this study, there is one major difference in the experimental techniques. The ion beam detection system employed in Okuno work is a channeltron. One ion beam is measured at a time, and the count rate is recorded for each beam individually. Whereas, in this work, a position sensitive detector is used, and the position of the beam spots can be viewed to ensure all beam is on the detector throughout the run. Also in this work, primary, and single capture beams can be measured simultaneously. This difference could possibly explain the differences in the measured values for the cross sections.

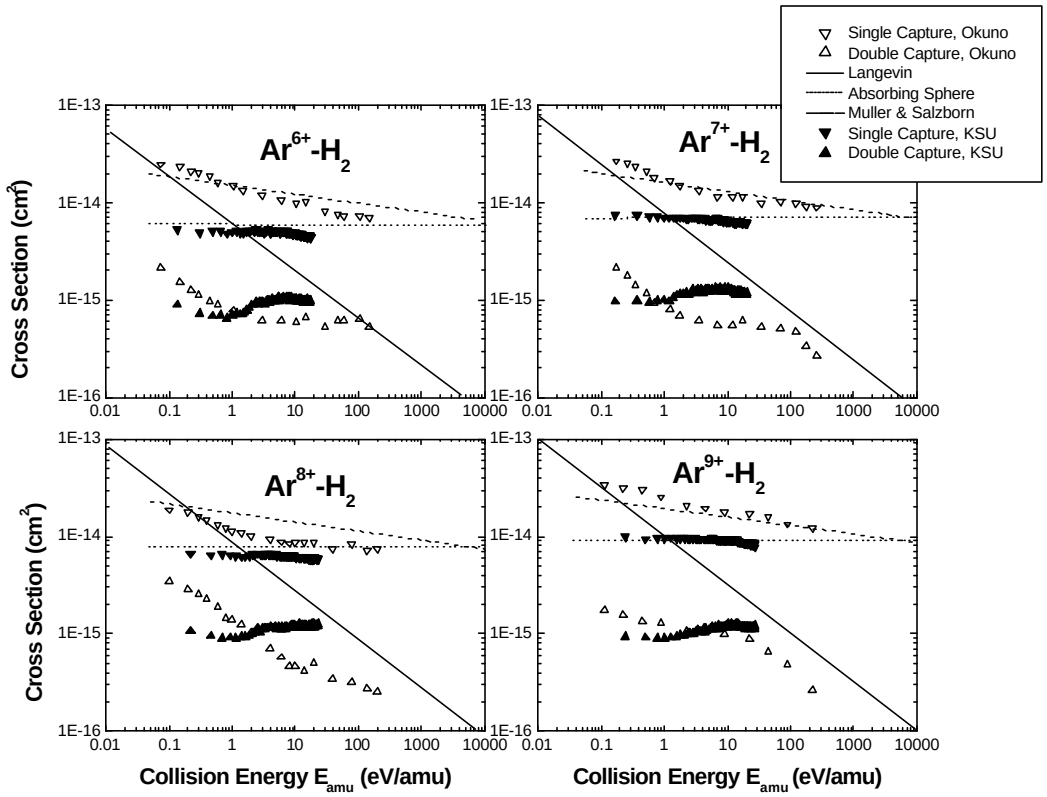

Figure 4.3 A representative graph for comparison between cross sections measured (with statistical error included) at Kansas State University and those of Okuno, and three simple theoretical models, displaying total single and double electron capture cross sections versus the collision energy in the laboratory frame for $Ar^{(6\text{-}9)+}$ on H_2.

While there is a very limited amount of data to compare the results of this study too, it is possible to compare the cross sections with those measured at higher energies. Single capture cross sections from this work are compared with other experimental data **[4.8]** at slightly higher energies for the $N^{7+} + H_2$ system in **Figure 4.4**.

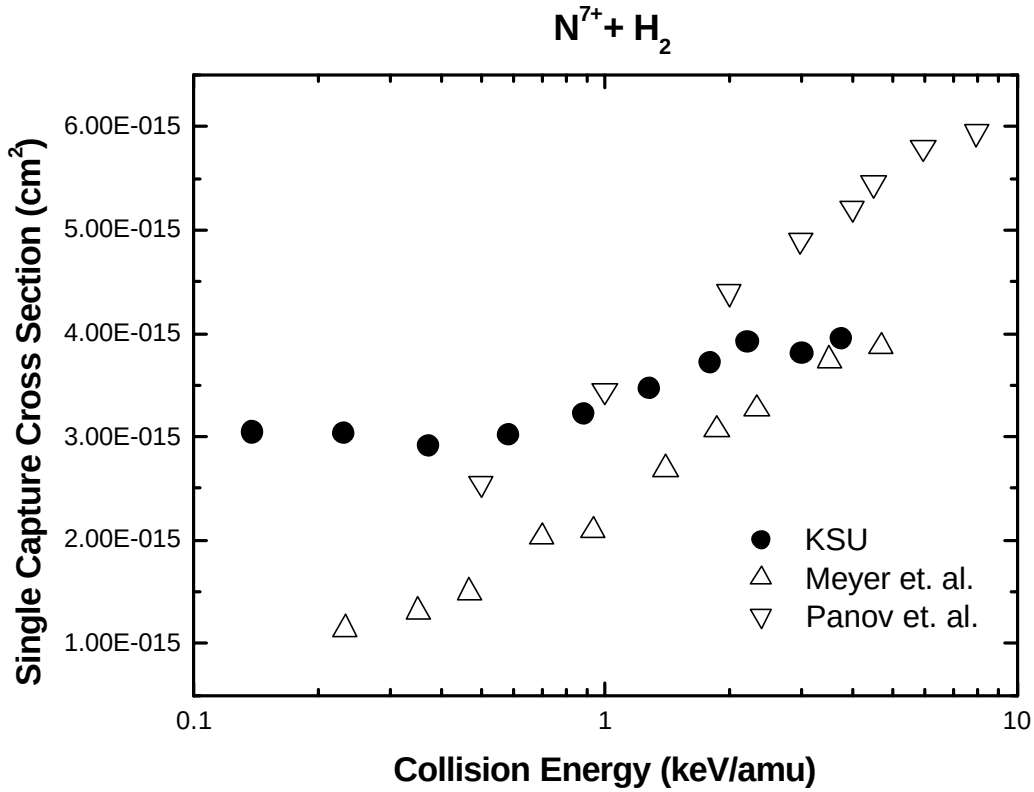

Figure 4.4 Single capture cross section from this study compared with single capture cross sections measured by Meyer, and Panov for the $N^{7+} + H_2$ system.

The single capture cross sections of this study fall between the single capture cross sections measured by Meyer and Panov. This is a result that illustrates that the **OPIG** produces results that are more or less consistent with measurements of others.

Others have measured cross sections are higher energies, and the single capture cross sections from those experiments are summarized in the list below.

Ion-atom system:	Energy:	Single Capture cross section:	Reference:
Ar^{5+} + He	1000qV	1.6×10^{-15} cm^2	4.1
Ar^{6+} + He	1000qV	2.1×10^{-15} cm^2	4.1
Ar^{7+} + He	1000qV	1.9×10^{-15} cm^2	4.1
Ar^{8+} + He	1000qV	1.8×10^{-15} cm^2	4.1
Ar^{9+} + He	1000qV	2.2×10^{-15} cm^2	4.1
Ne^{5+} + He	1000qV	1.8×10^{-15} cm^2	4.1
Ne^{6+} + He	1000qV	1.0×10^{-15} cm^2	4.1
Ne^{7+} + He	1000qV	2.8×10^{-15} cm^2	4.1
Ne^{8+} + He	1000qV	1.7×10^{-15} cm^2	4.1
Ne^{5+} + H_2	1000qV	4×10^{-15} cm^2	4.9
Ne^{6+} + H_2	1000qV	4×10^{-14} cm^2	4.9
Ar^{5+} + H_2	1000qV	2×10^{-15} cm^2	4.9
Ar^{6+} + H_2	1000qV	5×10^{-15} cm^2	4.9
Ar^{7+} + H_2	1000qV	5×10^{-15} cm^2	4.9
Ar^{8+} + H_2	1000qV	4.5×10^{-15} cm^2	4.9
Ar^{9+} + H_2	1000qV	7×10^{-15} cm^2	4.9

The cross sections in this list can be used to compare with the cross sections obtained in this study. Although the cross sections in the list are for higher energy measurements, the cross sections are generally in agreement with the magnitude of the cross sections measured in this study.

All of the measurements in the following sections are single and double electron capture cross sections measured in this work, and are compared with the extended classical over barrier model. As discussed earlier, the ion beam has a spread in energy. Because of this spread, there is a limit in collision energy, below which confidence in cross section results is reduced. In **Figure 4.5** through **Figure 4.31** a vertical bar is drawn indicating this limit. The bar is set at twice the energy spread of the ion beam for each case. Also, the single electron capture fraction is listed in the figure captions, and can be used to estimate the fraction of double capture that is due to double collisions.

1. $Ar^{(5\text{-}11)+}$ + He, H_2 Measurements

The single and double electron capture cross sections were systematically measured for projectile ions $Ar^{(5\text{-}11)+}$ incident on both He and H_2 targets. The results of these measurements are presented in this section.

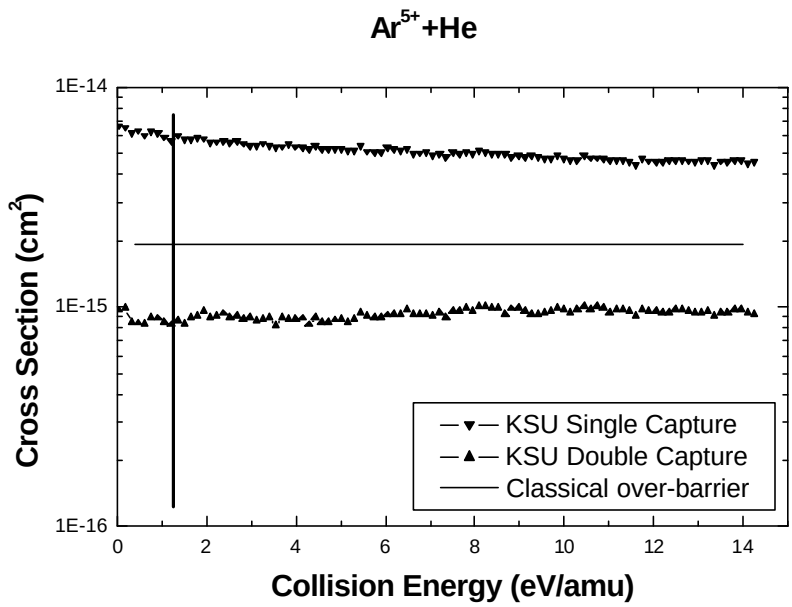

Figure 4.5 Total single and double electron capture cross sections plotted versus collision energy for Ar^{5+} + He. The solid line is the single capture classical over-barrier model. (The single capture fraction is 6 %).

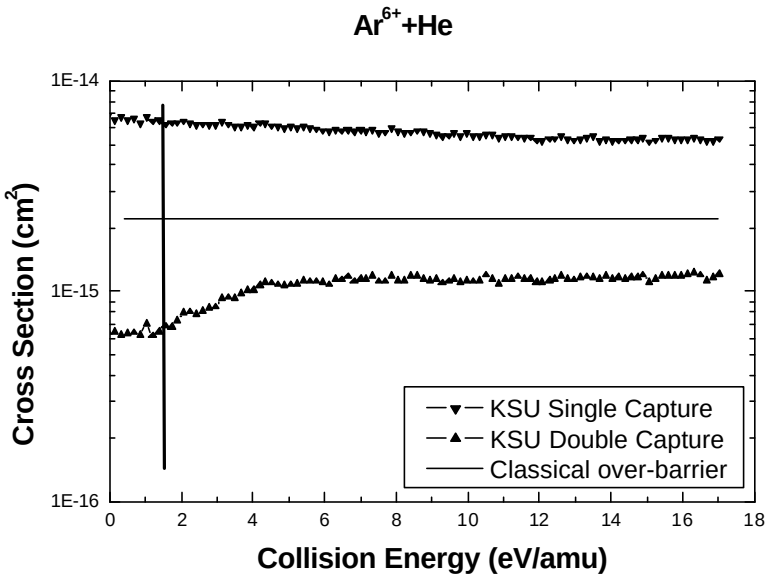

Figure 4.6 Total single and double electron capture cross sections plotted versus collision energy for Ar^{6+} + He. The solid line is the single capture classical over-barrier model. (The single capture fraction is 6 %).

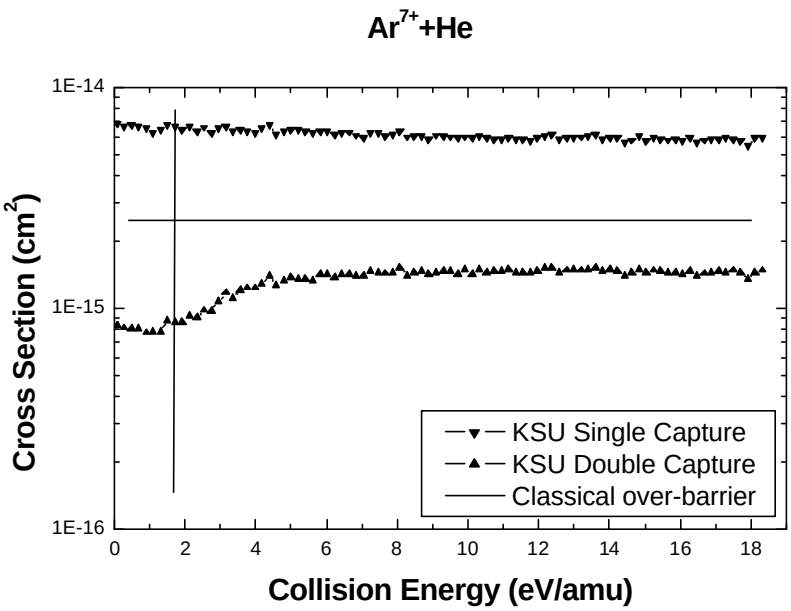

Figure 4.7 Total single and double electron capture cross sections plotted versus collision energy for Ar^{7+} + He. The solid line is the single capture classical over-barrier model. (The single capture fraction is 7.5 %).

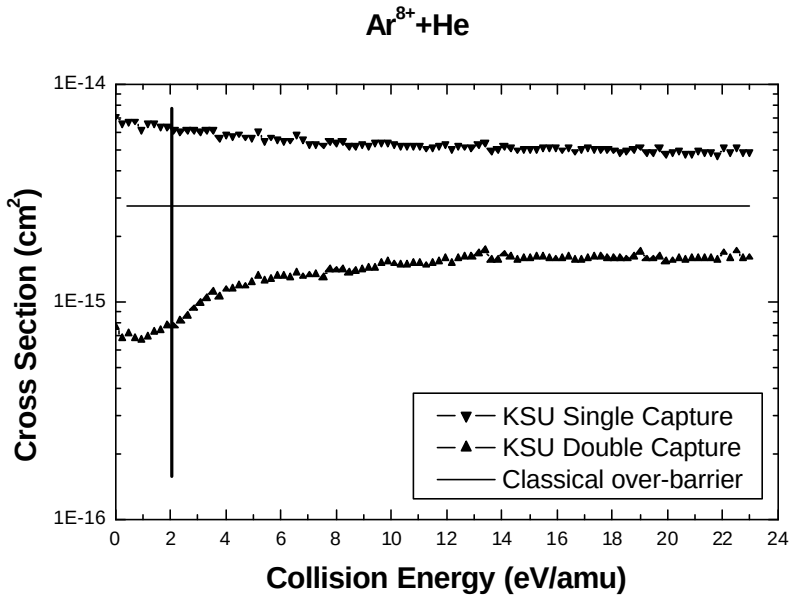

Figure 4.8 Total single and double electron capture cross sections plotted versus collision energy for Ar^{8+} + He. The solid line is the single capture classical over-barrier model. (The single capture fraction is 6 %).

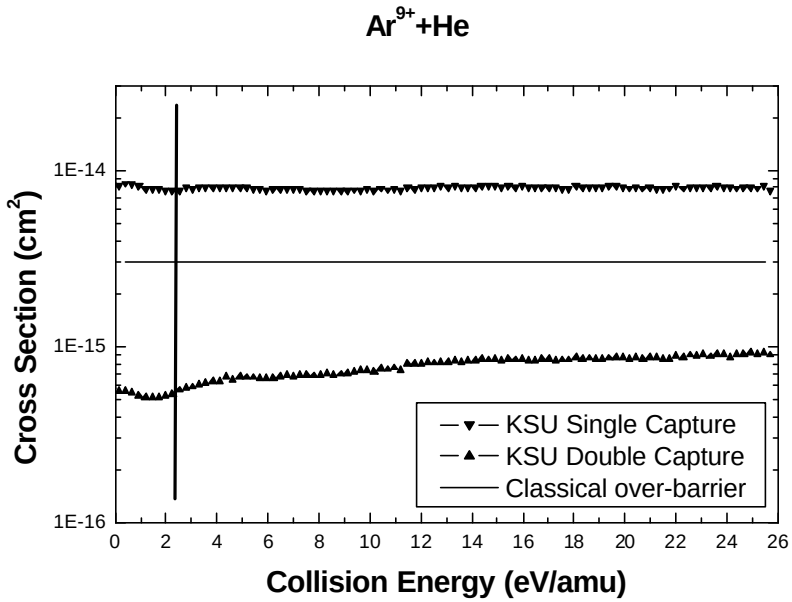

Figure 4.9 Total single and double electron capture cross sections plotted versus collision energy for Ar^{9+} + He. The solid line is the single capture classical over-barrier model. (The single capture fraction is 10 %).

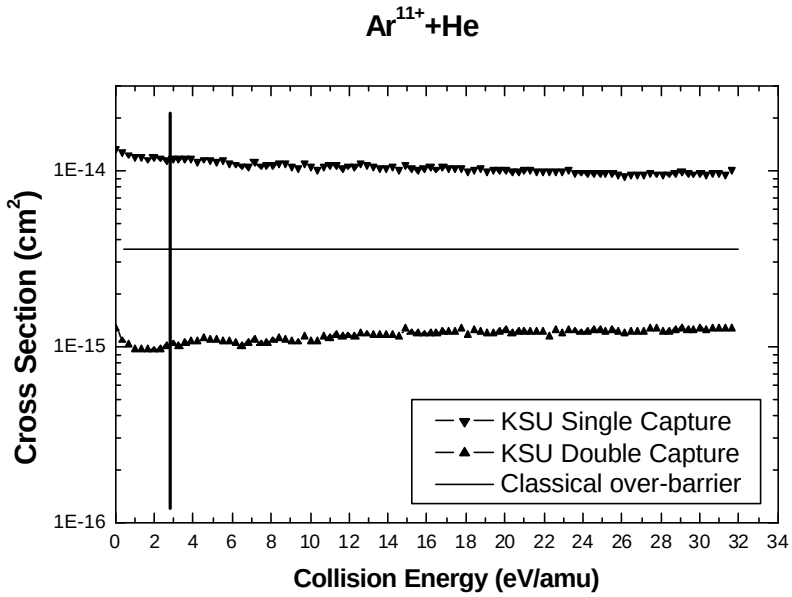

Figure 4.10 Total single and double electron capture cross sections plotted versus collision energy for Ar^{11+} + He. The solid line is the single capture classical over-barrier model. (The single capture fraction is 10 %).

Examining the cross section trends in **Figure 4.5** through **Figure 4.10**, it is clear that the single electron capture cross sections are quite flat as a function of the collision energy. The Niehaus extended classical over-barrier model predicts cross sections for these systems that are in fairly good agreement with the cross sections measured in this work (the COBM cross section under-estimates the measured cross sections by about a factor 2-3). Cross sections were calculated using the **COBM**, at one particular energy for $Ar^{(5\text{-}11)+}$ incident in He, but, for comparison purposes, can be considered as representative of the **COBM** cross section for the entire range of energy shown since the model is essentially independent of energy. The single electron **COBM** cross sections for the 5, 6, 7, 8, 9, and 11 charge states of Ar on He are 1.94, 2.21, 2.49, 2.76, 3.03, and 3.58×10^{-15}

cm^2 respectively. By solving **Equation 2.10**, the *n*-level that the electron is captured into on the projectile can be calculated. The extended over-barrier model has incorporated a distribution into the *n*-levels that electrons can capture into. In this way, the states that the electrons are captured into, has been calculated for the systems measured in this work. Most of the electrons captured by the projectile for the Ar^{5+} and Ar^{6+} on He systems go to the n=3 state. For Ar^{7+} on He, capture is shared between the n= 3, and n=4 channels, but the n=4 state receives a greater population. The Ar^{8+} on He system's main capture channel is the n=4 state. The Ar^{9+} on He system has electron capture somewhat evenly distributed between the n=4 and n=5 states. The Ar^{11+} on He system has electron capture to the n=5 and n=6 states, with the n=5 state being the more dominant.

In some cases it appears that there is a gentle increase in the single electron capture cross section with decreasing energy near the low energy end of the data, which suggests there may be a small contribution to the cross section due to a Langevin type of interaction, where the polarization of the target atom begins to influence the trajectory of the projectile, and large impact parameters can result in relatively small distances of closest approach to the target atom, which leads to an increase in the probability of capture.

The cross section measurements taken with hydrogen as a target have the same characteristics as the measurements taken with helium, but are in closer agreement with the classical over-barrier model. The measured cross sections using hydrogen as a target are shown in **Figure 4.11** through **Figure 4.16**.

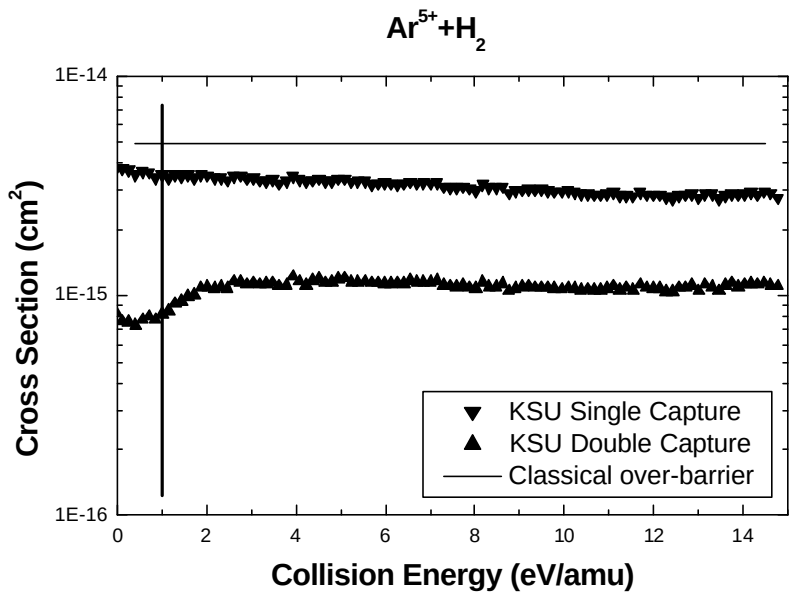

Figure 4.11 Total single and double electron capture cross sections plotted versus collision energy for $Ar^{5+} + H_2$. The solid line is the single capture classical over-barrier model. (The single capture fraction is 5 %).

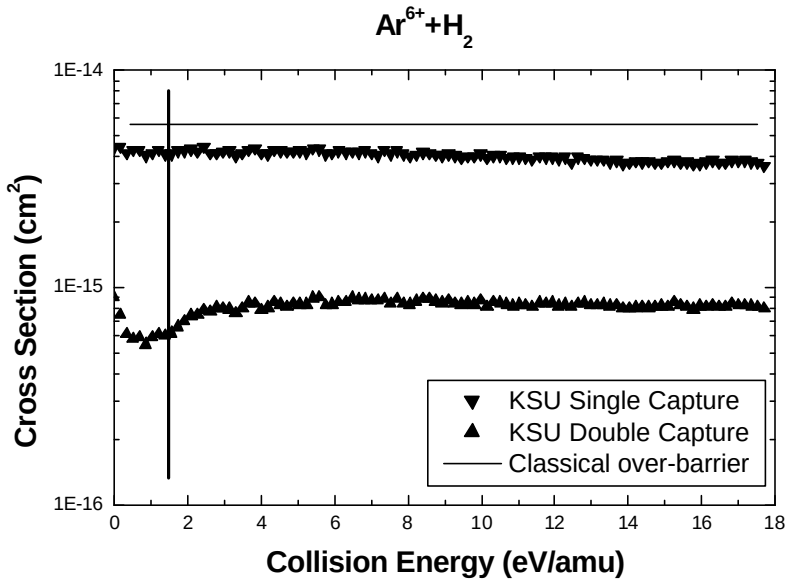

Figure 4.12 Total single and double electron capture cross sections plotted versus collision energy for $Ar^{6+} + H_2$. The solid line is the single capture classical over-barrier model. (The single capture fraction is 5 %).

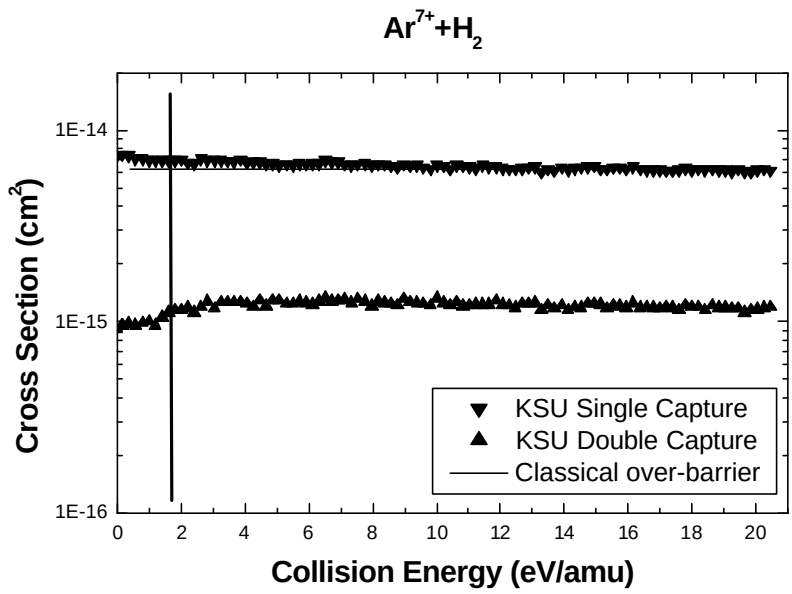

Figure 4.13 Total single and double electron capture cross sections plotted versus collision energy for $Ar^{7+} + H_2$. The solid line is the single capture classical over-barrier model. (The single capture fraction is 12 %).

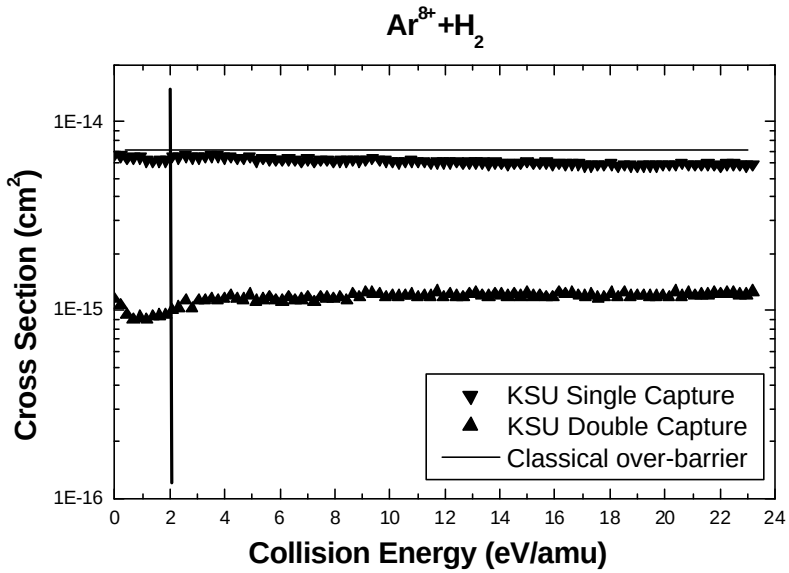

Figure 4.14 Total single and double electron capture cross sections plotted versus collision energy for $Ar^{8+} + H_2$. The solid line is the single capture classical over-barrier model. (The single capture fraction is 7.5 %).

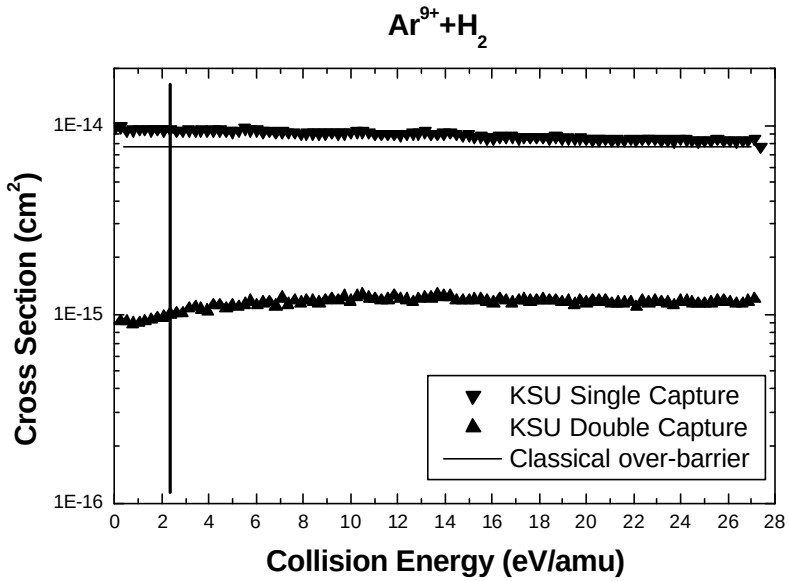

Figure 4.15 Total single and double electron capture cross sections plotted versus collision energy for $Ar^{9+} + H_2$. The solid line is the single capture classical over-barrier model. (The single capture fraction is 13 %).

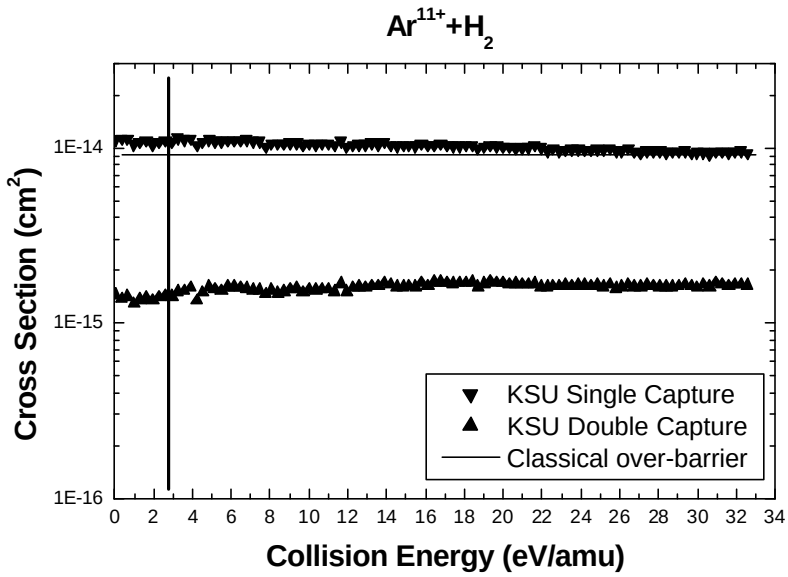

Figure 4.16 Total single and double electron capture cross sections plotted versus collision energy for $Ar^{11+} + H_2$. The solid line is the single capture classical over-barrier model. (The single capture fraction is 15 %).

The cross sections using a hydrogen target show some variation at energies below 2 eV/amu, particularly for the double electron capture cross sections, but are essentially flat through most of the energy range covered. The Ar^{5+} on H_2 system has electron capture shared nearly equally by the n=3 and n=4 states. The Ar^{6+} on H_2 system captures mainly into the n=4 state. For the Ar^{7+} and Ar^{8+} on H_2 systems, the dominant capture channel is to the n=5 state. The Ar^{9+} on H_2 system, has electron capture mainly to the n=6 state, and the Ar^{11+} on H_2 system has a main capture channel into the n=7 level.

2. $N^{(3-7)+}$ + H_2 Measurements

$N^{(3-7)+}$ ions were used as projectiles incident on a H_2 target, yielding the following results. Comparison of the measured single capture cross sections with the classical over-barrier model showed good agreement for all systems of this ion species, with the exception of N^{3+}, where the classical over-barrier model cross section was a little more than two times what was measured experimentally. The double capture to single capture cross section ratio for the N^{3+} on H_2 measurement is approximately 0.5, which is much higher than for the other projectile ion charge states used, for which the average ratio was approximately 0.1. Again, the basic trends are the same for this series of systems measured. The single and double capture cross sections are roughly constant over the energy range studied, but do exhibit some variations at energies below 5 eV/amu.

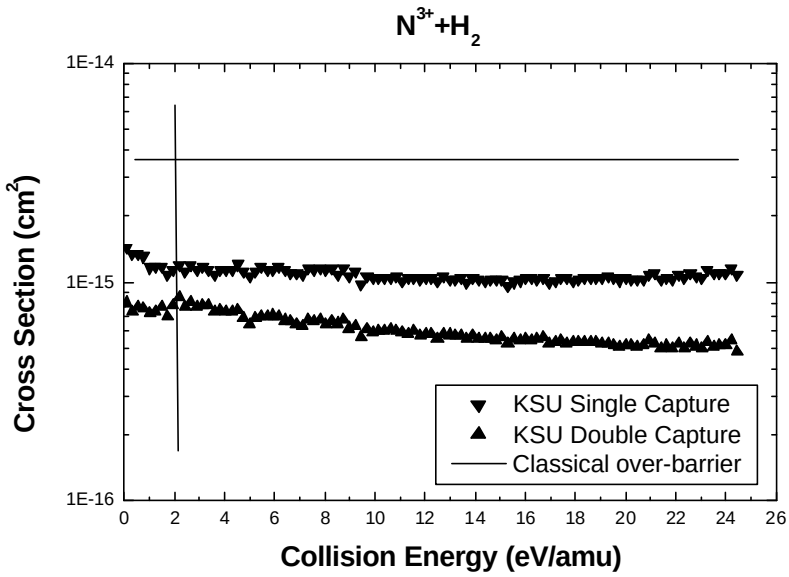

Figure 4.17 Total single and double electron capture cross sections plotted versus collision energy for $N^{3+} + H_2$. The solid line is the single capture classical over-barrier model. (The single capture fraction is 2.5 %).

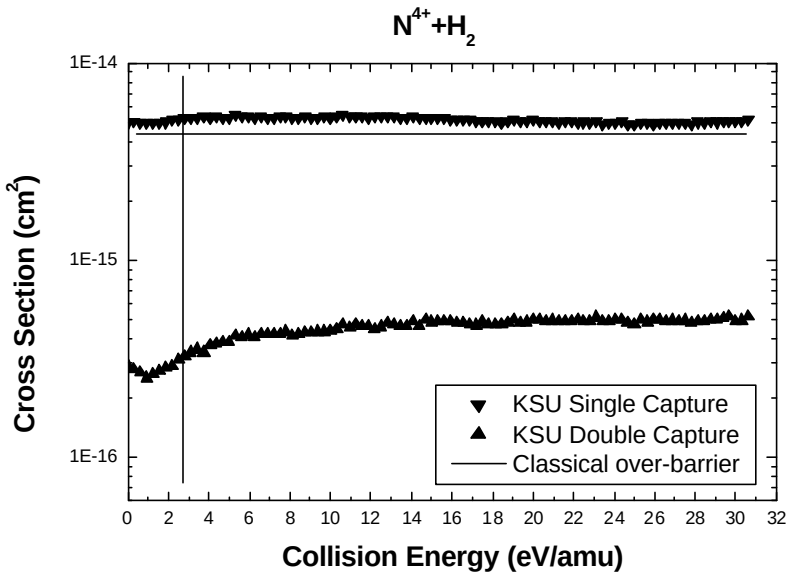

Figure 4.18 Total single and double electron capture cross sections plotted versus collision energy for $N^{4+} + H_2$. The solid line is the single capture classical over-barrier model. (The single capture fraction is 12 %).

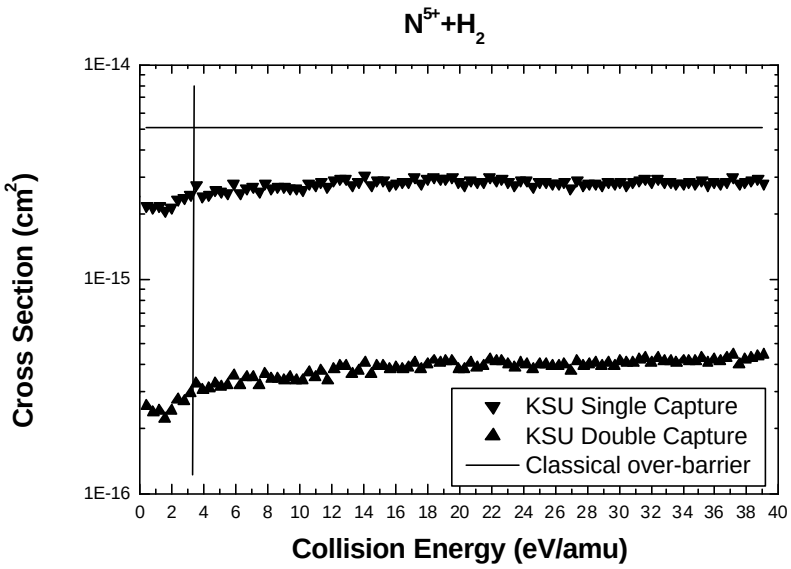

Figure 4.19 Total single and double electron capture cross sections plotted versus collision energy for $N^{5+} + H_2$. The solid line is the single capture classical over-barrier model. (The single capture fraction is 7 %).

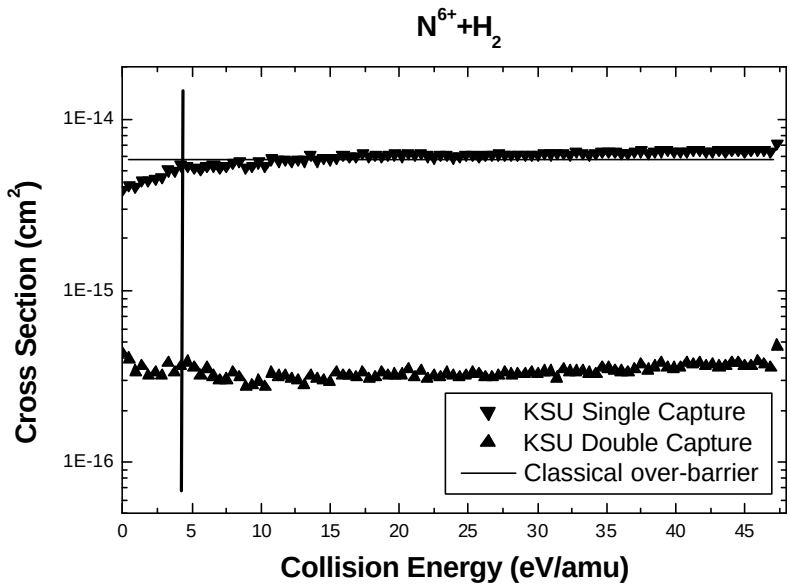

Figure 4.20 Total single and double electron capture cross sections plotted versus collision energy for $N^{6+} + H_2$. The solid line is the single capture classical over-barrier model. (The single capture fraction is 15 %).

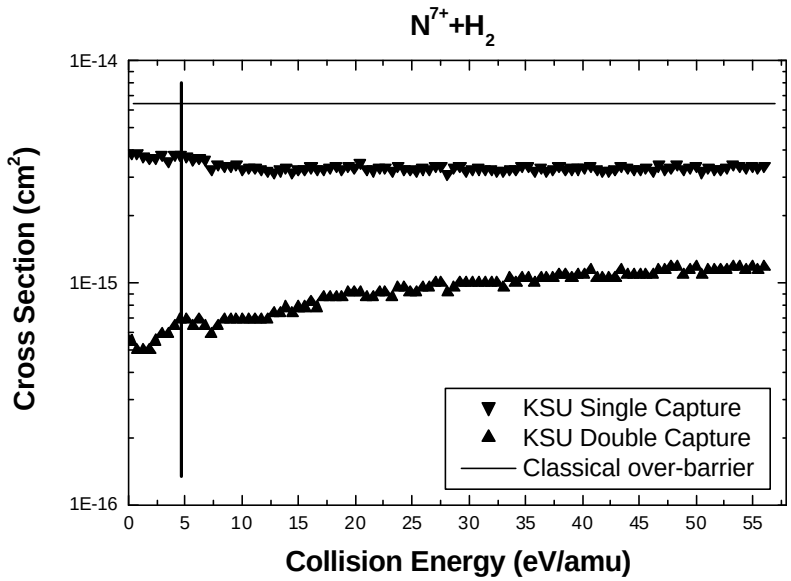

Figure 4.21 Total single and double electron capture cross sections plotted versus collision energy for $N^{7+} + H_2$. The solid line is the single capture classical over-barrier model. (The single capture fraction is 7.5 %).

For the N^{3+}on H_2 system, the over-barrier model predicts that electrons will be captured mainly into the n=2 and partially into the n=3 levels of the projectile ion. The N^{4+}on H_2 system has electron capture going predominantly into the n=3 level. Electron capture is shared between the n=3, and n=4 levels, for the N^{5+}on H_2 system. The N^{6+}on H_2 system has capture going primarily into the n=4 level, and for the N^{7+}on H_2 system, electron capture is shared between the n=4, and n=5 levels.

3. $Ne^{(5\text{-}9)+}$ + He Measurements

The measured single and double electron capture cross sections for $Ne^{(5\text{-}9)+}$ on He are shown in **Figures 4.22** through **4.26**. The cross sections in this series of measurements was perhaps the most interesting, due to the fact that the cross sections were not always constant as a function of collision energy. Each of these runs was repeated, to ensure that the apparent change in the cross sections with collision energy was genuine, rather than the effect of some kind of systematic error. While the single capture cross sections were essentially independent of collision energy throughout the energy range measured, the double capture cross sections increased quite dramatically at collision energies below 5 eV/amu for the $Ne^{(7\text{-}9)+}$ on He collision systems. The double electron capture cross section for the Ne^{6+} on He collision system decreased at collision energies below 5 eV/amu.

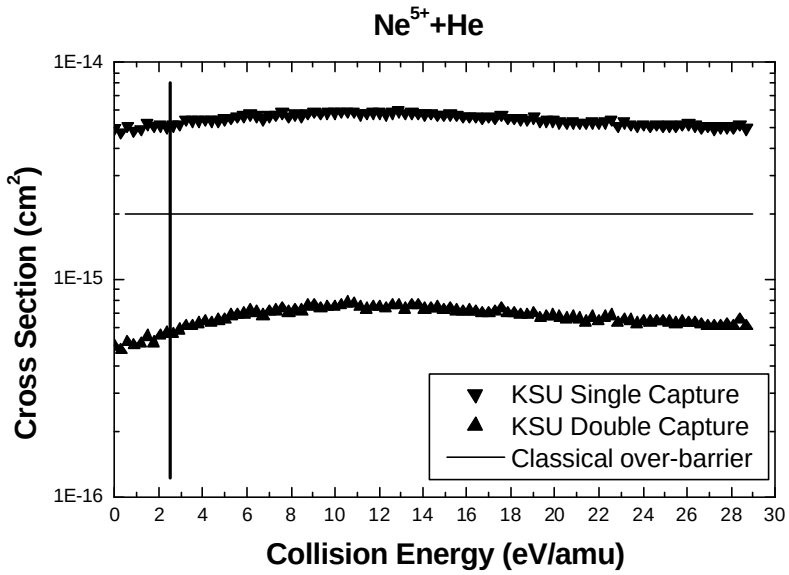

Figure 4.22 Total single and double electron capture cross sections plotted versus collision energy for Ne^{5+} + He. The solid line is the single capture classical over-barrier model. (The single capture fraction is 7.5 %).

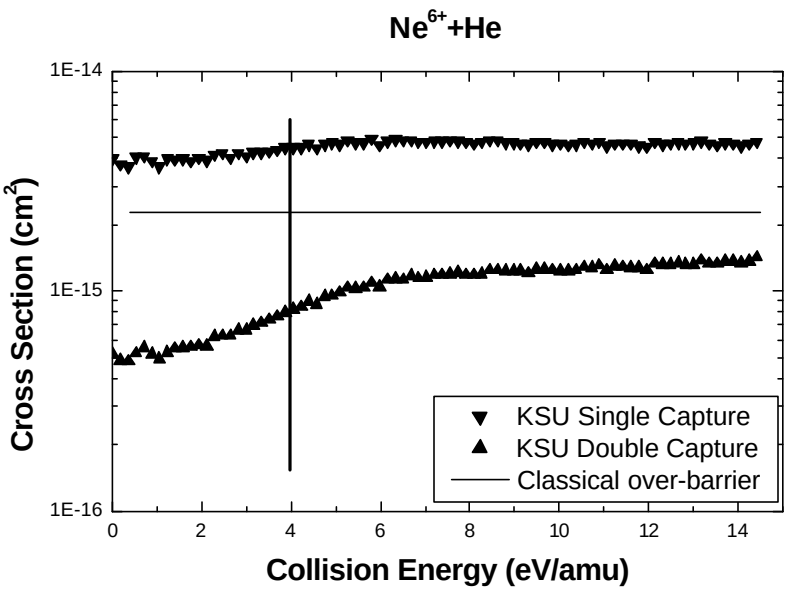

Figure 4.23 Total single and double electron capture cross sections plotted versus collision energy for Ne^{6+} + He. The solid line is the single capture classical over-barrier model. (The single capture fraction is 7.5 %).

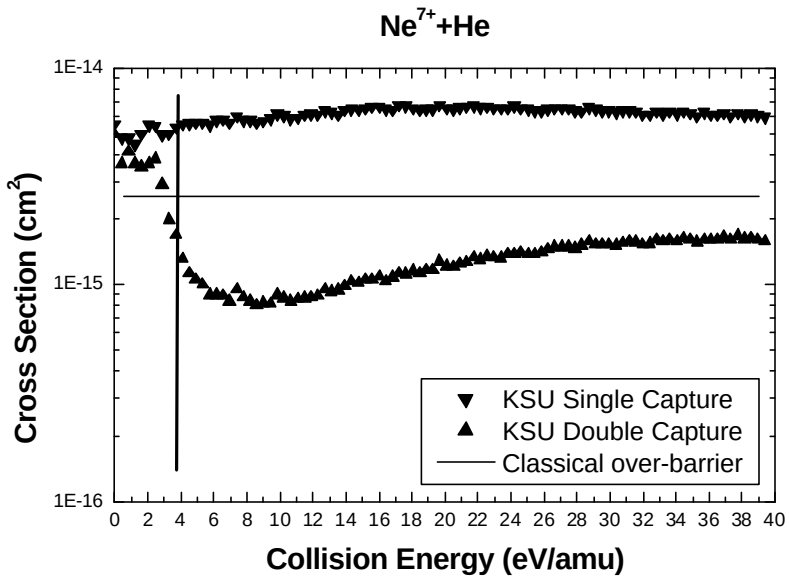

Figure 4.24 Total single and double electron capture cross sections plotted versus collision energy for Ne^{7+} + He. The solid line is the single capture classical over-barrier model. (The single capture fraction is 9 %).

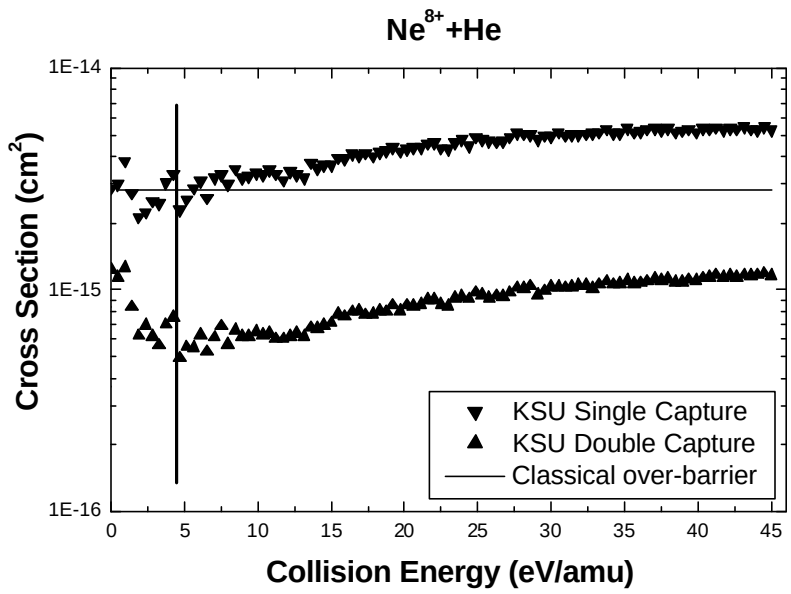

Figure 4.25 Total single and double electron capture cross sections plotted versus collision energy for Ne^{8+} + He. The solid line is the single capture classical over-barrier model. (The single capture fraction is 7.5 %).

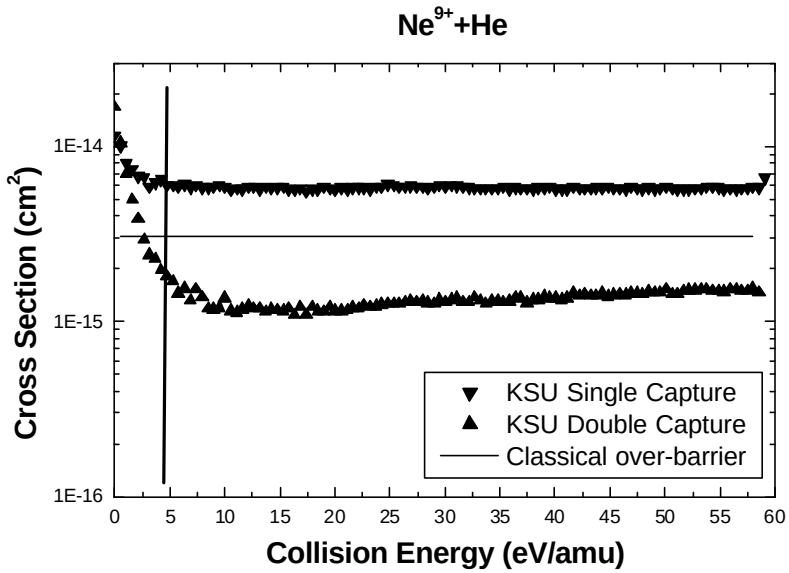

Figure 4.26 Total single and double electron capture cross sections plotted versus collision energy for Ne^{9+} + He. The solid line is the single capture classical over-barrier model. (The single capture fraction is 8 %).

The over-barrier model, single capture cross sections were in fairly good agreement with this series of cross sections measurements. The $Ne^{5,6+}$ on He systems had electron capture mainly into the n=3 level. The $Ne^{7,8+}$ on He systems had capture primarily into the n=4 level, and the Ne^{9+} + He system had capture into both the n=4 and n=5 levels.

4. O^{2+} + He, H_2, Ar, Ne Measurements

Another study that was done, was the series of measurements, in which the ion species and charge state was kept the same, and the only the target was varied. O^{2+} was

used as the projectile ion for this series of measurements, and the targets used were He, H_2, Ar, and Ne. Since the **OPIG** only guides ions through the gas cell, double capture could not be measured. (It results in a neutral beam). One reason O^{2+} was chosen as a projectile ion was to test cross section behavior for low charge state projectile ions.

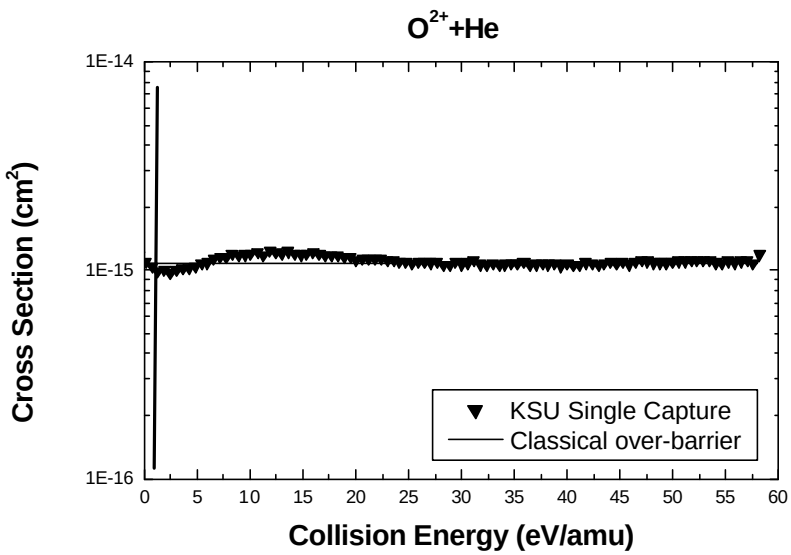

Figure 4.27 Total single electron capture cross section plotted versus collision energy for O^{2+} + He. The solid line is the single capture classical over-barrier model. (The single capture fraction is 9 %).

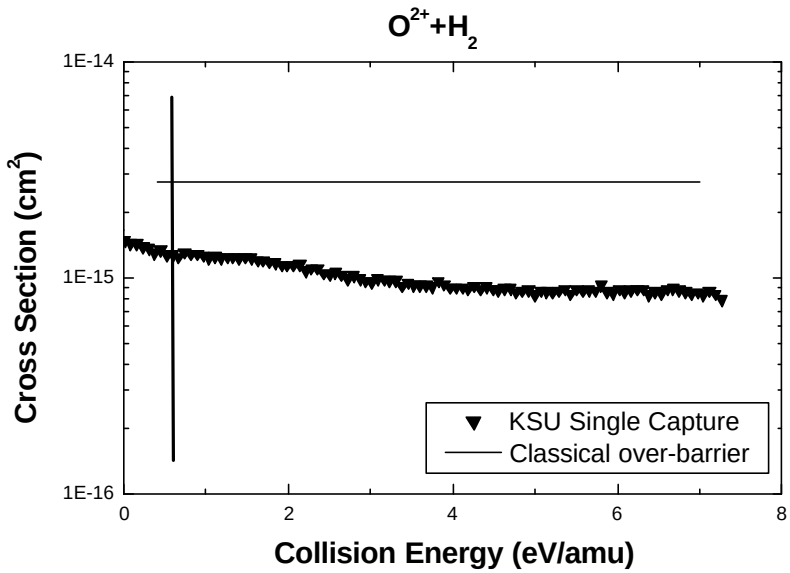

Figure 4.28 Total single electron capture cross section plotted versus collision energy $O^{2+} + H_2$. The solid line is the single capture classical over-barrier model. (The single capture fraction is 6 %).

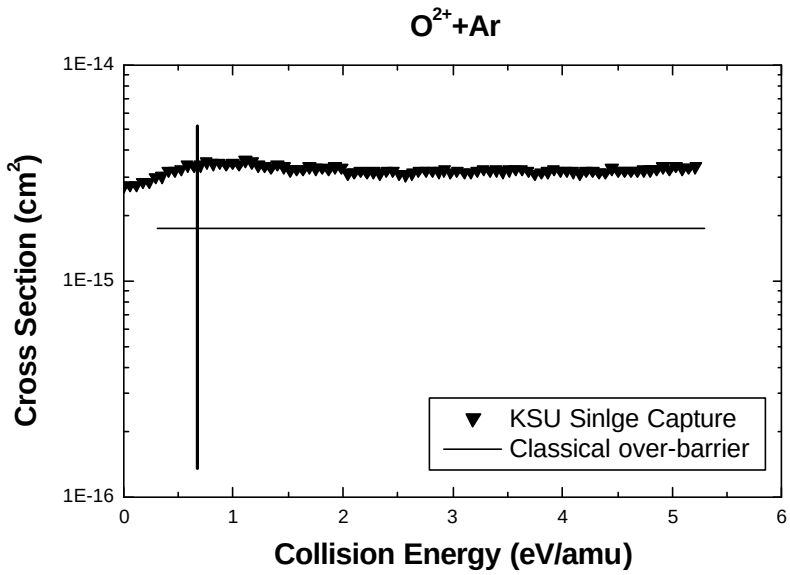

Figure 4.29 Total single electron capture cross section plotted versus collision energy O^{2+} + Ar. The solid line is the single capture classical over-barrier model. (The single capture fraction is 7.5 %).

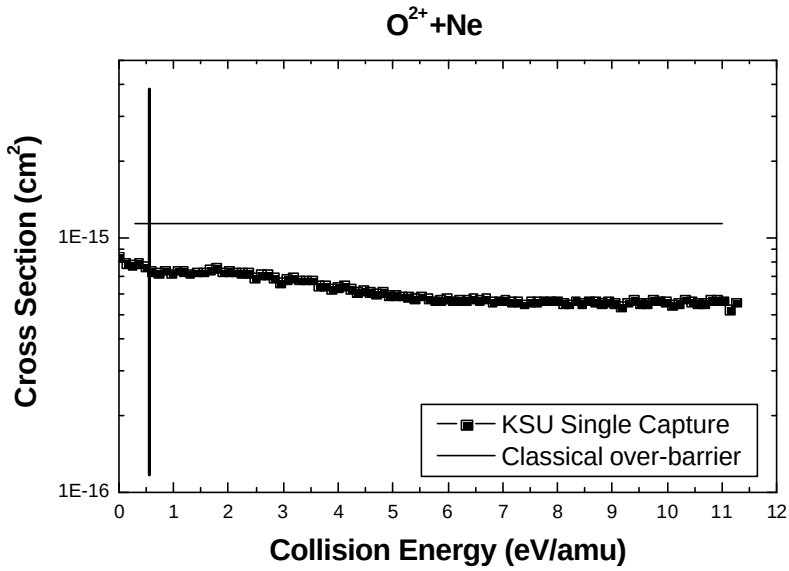

Figure 4.30 Total single electron capture cross section plotted versus collision energy O^{2+} + Ne. The solid line is the single capture classical over-barrier model. (The single capture fraction is 4 %).

Electron capture by the projectile ion is shared between the n=1 and n=2 states for O^{2+} on He and H_2 and Ne. Electron capture is into the n=2 state with an Ar target.

5. Xe^{26+} + H_2 Measurements

In **Figure 4.31**, comparing the basic over-barrier model single capture cross section with the measured single capture cross section for the Xe^{26+} on H_2 system, the basic over-barrier model overestimates the measured cross section by a little less than a factor of 2.

The same trends that have been observed for most of the other systems measured are also present in this measurement. Both the single and double electron capture cross

sections are essentially constant as functions of collision energy for the energy range studied. The single capture cross section is about 2 times as great as that for double capture. This is a relatively high double to single electron capture cross section ratio, but is not too surprising since the projectile ion has a much deeper potential well than for the other systems measured.

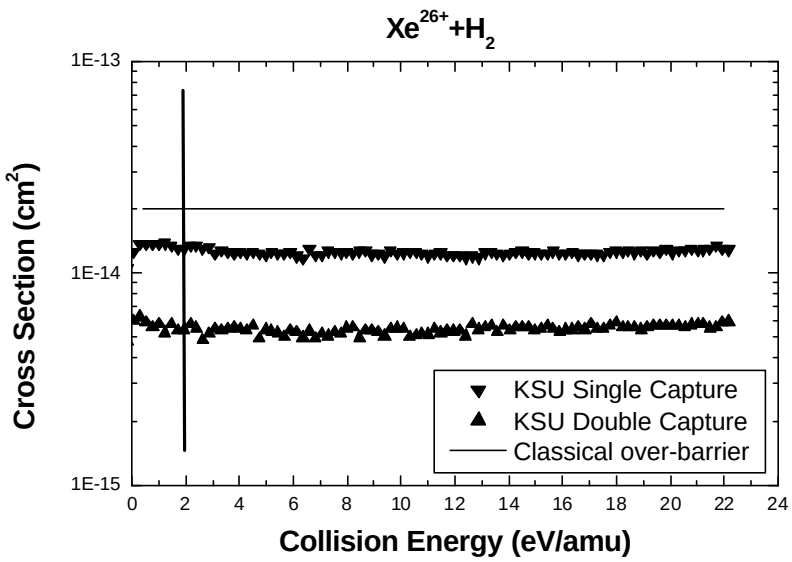

Figure 4.31 Total single and double electron capture cross sections plotted versus collision energy $Xe^{26+} + H_2$. The solid line is the single capture classical over-barrier model (simple model).